Statistics and dynamics of a liquid jet under fragmentation by a gas jet

Oliver Tolfts, Guillaume Deplus, and Nathanaël Machicoane ⬥[*]

Univ. Grenoble Alpes, CNRS, Grenoble INP, LEGI, 38000 Grenoble, France

The breakup of a liquid jet by a surrounding gas jet is studied in a coaxial configuration using high-speed back-lit imaging. This work focuses on the time dynamics and the statistics of the length of the liquid jet. The inlet velocities are varied for both fluids to obtain a wide range of gas and liquid Reynolds numbers and equivalently a wide range of gas-to-liquid dynamic pressure ratio M and Weber number. The variety of scales exhibited throughout this range, exploring two breakup regimes, is covered by adapting the spatial and temporal resolutions as well as the field of view of the imaging system. An in-depth study of the distributions of the length of the liquid jet is presented, with the associated scalings for the evolution of the first three statistical moments with the relevant dimensionless parameters, fully describing the statistics through a unique function. The first two moments of the distributions are shown to be power laws of M and their ratio is observed to be constant. The temporal dynamics are studied using autocorrelation functions of the length of the liquid jet. The correlation times are shown to be controlled by the gas jet, with a secondary influence of the liquid Reynolds number through a change of behavior that appears to be related to the onset of liquid turbulence. In addition, a transition between two regimes highlighted by a change of shape of both the probability density and autocorrelation functions of the liquid core length is introduced and its link to the turbulence characteristics of the gas jet and the underlying breakup mechanisms is discussed.

I. INTRODUCTION

The fragmentation of a liquid jet by a surrounding gas jet stands as a useful setting to study the fundamental mechanisms that take place in the transport, destabilization, and breakup of a liquid phase by a turbulent gas phase. This situation is at the base of gas-assisted, also called airblast, atomization, where atomization is defined as the breakup of a bulk of liquid into a cloud of droplets (spray). Atomization finds numerous applications in industry, e.g., combustion and manufacturing, but also in natural systems such as sea sprays [1–3]. In gas-assisted atomization, the interaction of a liquid jet with a surrounding high-speed gas jet leads to the fragmentation of the liquid phase into a spray through a cascade of destabilization and breakup mechanisms [4–9]. A Kelvin-Helmholtz instability was identified as being responsible for the initial disturbance of the liquid-gas interface [4,5,8,10,11]. This creates a wave-shaped perturbation on the surface of the liquid jet, which is then destabilized by the gas jet. The subsequent mechanism can be described by taking an analogy to the breakup of a single drop with no initial velocity and suddenly accelerated by a gas flow, as studied in Ref. [12] (alternatively readers can refer to the review of Theofanous [13]). They report different drop breakup mechanisms and classify them according to the Weber number We at the drop scale, which compares aerodynamic stresses to the drop surface tension force as

---

[*]nathanael.machicoane@univ-grenoble-alpes.fr

044304-1

We $= \rho_g U^2 d/\sigma$, where ρ_g is the gas density, U the relative velocity between the drop and the gas flow, d the drop diameter, and σ the surface tension coefficient. For low We values, they observed that the drop is first flattened into a disklike shape, surrounded by a thick liquid rim. As the disk is further stretched and inflated by the gas flow, it thins into a membrane that will eventually break into small droplets, while the rim produces larger droplets. This breakup regime is referred to as bag breakup or membrane breakup. For high values of the Weber number, the drop initially flattens and the drop's interface, roughly transverse to the gas flow, is strongly accelerated, leading to a Rayleigh-Taylor instability. When the amplitude of this instability reaches the width of the flattened drop, it breaks into droplets. This breakup regime is referred to as catastrophic breakup. A similar classification of the qualitative visualization of the breakup of a liquid jet by a surrounding gas jet has been done [14,15]. For low gas velocities, the wave-shaped perturbation is inflated, creating a thin membrane that will eventually break into droplets [16]. For higher gas velocities, the wave-shaped perturbation is stretched into a ligament that can detach from the liquid bulk, or undergo Rayleigh-Taylor instability, leading to the formation of drops peeled off from the liquid jet. Both of these underlying breakup mechanisms define breakup regimes, respectively called membrane-breakup (alternatively bag-breakup) regime, and fiber-type atomization (alternatively stripping regime) [15]. In addition to the small-scale breakup mechanisms, a large-scale motion of the entire liquid jet can take a role in the cascade of breakup mechanisms. This large-scale instability is referred to as flapping [7,17–19]. Each breakup mechanism participates in the fullness of the size and spatiotemporal distributions of the resulting droplets that form the spray.

The fragmentation of a liquid jet by a surrounding gas jet is a turbulent two-phase flow involving a wide range of temporal and spatial scales. The multiscale nature of spray formation prevents using a single approach to study the underlying mechanisms of the fragmentation cascade. Such complexity coupled with the broad scope of applications involving sprays led to the introduction of many dimensionless controlling parameters and reported metrics. The liquid core length L_B, defined as the longitudinal extent of the portion of liquid that is connected to the nozzle, stands as one of the first metrics that comes to mind and received attention early on in coaxial atomization [20]. Focusing on the average liquid core length, the gas-to-liquid dynamic pressure ratio M was identified as the driving parameter [17,21,22]. Using different fluids, geometries, and varying the velocity of the fluids at the injection, Ref. [21] proposed a power-law decay with M. References [17,22] reported a similar exponent along M, confirming the scaling and identifying that the prefactor of the power law was influenced by the nozzle geometry. Modest interest has been given to the fluctuations of L_B. The ratio of the standard deviation to the average liquid core length was reported in Refs. [17,23]. Recent studies have looked deeper into the statistics by describing the probability density function of L_B [19,24], showing non-Gaussian behaviors. One could expect that the change in breakup regimes described above has a signature on the behavior of L_B. Nevertheless, to our best knowledge, no quantitative indicator of the change of breakup regime has yet been found when studying the liquid core length.

Considering temporal scales involved in spray formation processes, the flapping instability frequency was shown to be mostly governed by the gas jet velocity [7]. In addition, the inner vorticity layer of the annular gas jet was reported to directly influence the frequency of the Kelvin-Helmholtz and Rayleigh-Taylor instabilities [4,5]. The timescale of the liquid core length was recently extracted using autocorrelation functions [24,25]. Both studies conclude that the timescale diminishes with M but only the gas velocity was varied (constant laminar liquid injection). Since the gas jet is at the origin of the destabilization and breakup of the liquid jet, one can expect the timescales of the gas flow to drive the timescales of L_B. However, no study was pursued on the role of the liquid Reynolds number and of the onset of liquid turbulence on the temporal dynamics of the liquid core length.

The present work aims at addressing the questions raised on the effect of breakup regime and liquid turbulence on the behavior of the liquid core length, through the introduction of a framework that adequately describes its statistics and temporal dynamics. Therefore, an experimental study is conducted on a wide range of liquid and gas Reynolds numbers, encompassing two breakup regimes and the transition from a laminar to a turbulent state of the liquid jet, resulting in over four orders of

magnitude of variation of the gas-to-liquid dynamic pressure ratio M. While M appears to govern the evolution of the mean liquid core length along variations of injection parameters, the qualitative boundary between the membrane-breakup and fiber-type atomization regimes is almost vertical in the $\{Re_l; We_g\}$ parameter space [15]. Re_l stands here for the Reynolds number of the liquid jet (equivalently Re_g can be used for the gas jet), and We_g is the Weber number comparing the gas jet dynamic pressure to the surface tension force of the liquid jet. For a fixed couple of fluids, this means that the transition occurs at a given gas velocity. By increasing the gas velocity at several values of the liquid Reynolds number (liquid velocity), the explored parameter space crosses this transition many times at various values of M, giving the possibility to uncouple We_g (change of regimes) and M (scalings of L_B). An alternate approach would be to vary the parameters of the fluids (in particular the fluids densities and the surface tension coefficient) [21,26,27], which is more challenging in the current setup. In the approach where only the liquid and gas velocities are varied, the effects of the gas velocity are equivalently described by We_g and Re_g. First, the previous introduction of a functional description of the full statistics of L_B [19] is validated in the extended range of nondimensional parameters. This approach underlines a transition that is confirmed by the temporal behavior and can be related to changes in breakup regime. In addition, the timescales of the liquid core length are reported to scale linearly with the inverse of the gas mean exit velocity but also show an increased prefactor when the injected liquid jet is turbulent. Throughout the paper, changes in atomization regimes and the onset of liquid turbulence are highlighted with the use of color bars and symbols (described accordingly in the captions of the figures), and the effect of both aspects on the statistics and temporal dynamics of the liquid core length are discussed in Sec. V. Section II first describes the experimental setup and the analyses. The statistics and temporal dynamics are respectively presented in Secs. III and IV. The discussion (Sec. V) is then followed by a conclusion (Sec. VI).

II. MATERIALS AND METHODS

A. Two-fluid coaxial atomizer

The experimental setup consists of a coaxial atomizer, shown in Fig. 1(a) (more details on the open-source geometry is given in Ref. [28]). The liquid nozzle is 100 mm long, with an inner diameter $d_l = 1.98$ mm and an outer diameter $D_l = 3.1$ mm. This geometry ensures a Poiseuille flow is fully established before the liquid exits the nozzle when operated in laminar conditions, while a fully developed plug flow is expected in turbulent conditions. The liquid nozzle is placed at the center of the gas nozzle. The outer wall of the liquid nozzle and the inner wall of the gas nozzle form a cavity that channels the gas into an annular exit plane with an inner diameter D_l and an outer diameter $d_g = 9.985$ mm. Note that d_l, D_l, and d_g are measured with the same accuracy of 1 μm. Both of these walls present a cubic-spline shape ensuring the gas flow is longitudinal when it exits the nozzle. The working fluids are air and water at 25 °C.

The volumetric flow rates of the gas and the liquid, respectively, noted Q_g and Q_l, are monitored by flowmeters. A pressurized tank is used to produce the liquid flow. The tank's pressure is regulated to limit the fluctuations in the flow rate. The uncertainty of the liquid flow rate is given by the uncertainty of the associated flowmeter $\Delta Q_l = 0.06$ l/min. Compressed air is used for the gas flow, with a pressure regulator set below the compressor's low-pressure point to ensure a steady gas flow. The uncertainty of the gas flow is dominated by the small variations caused by the feedback control loop that fixes the gas flow rate. This uncertainty, much larger than the flowmeter uncertainty, is calculated for each run and is typically of order $\Delta Q_g = 2.5$ l/min.

We define the gas and liquid mean velocities at the exit plane respectively as $U_g = \frac{Q_g}{A_g}$ and $U_l = \frac{Q_l}{A_l}$, with $A_l = \pi \frac{d_l^2}{4}$ the liquid section and $A_g = \frac{\pi}{4}(d_g^2 - D_l^2)$ the gas section. The liquid Reynolds number $Re_l = \frac{U_l d_l}{\nu_l}$, where ν_l is the kinematic viscosity of water, is varied from 730 to 20 000, encompassing the transition from a laminar to a turbulent exiting liquid jet. The gas
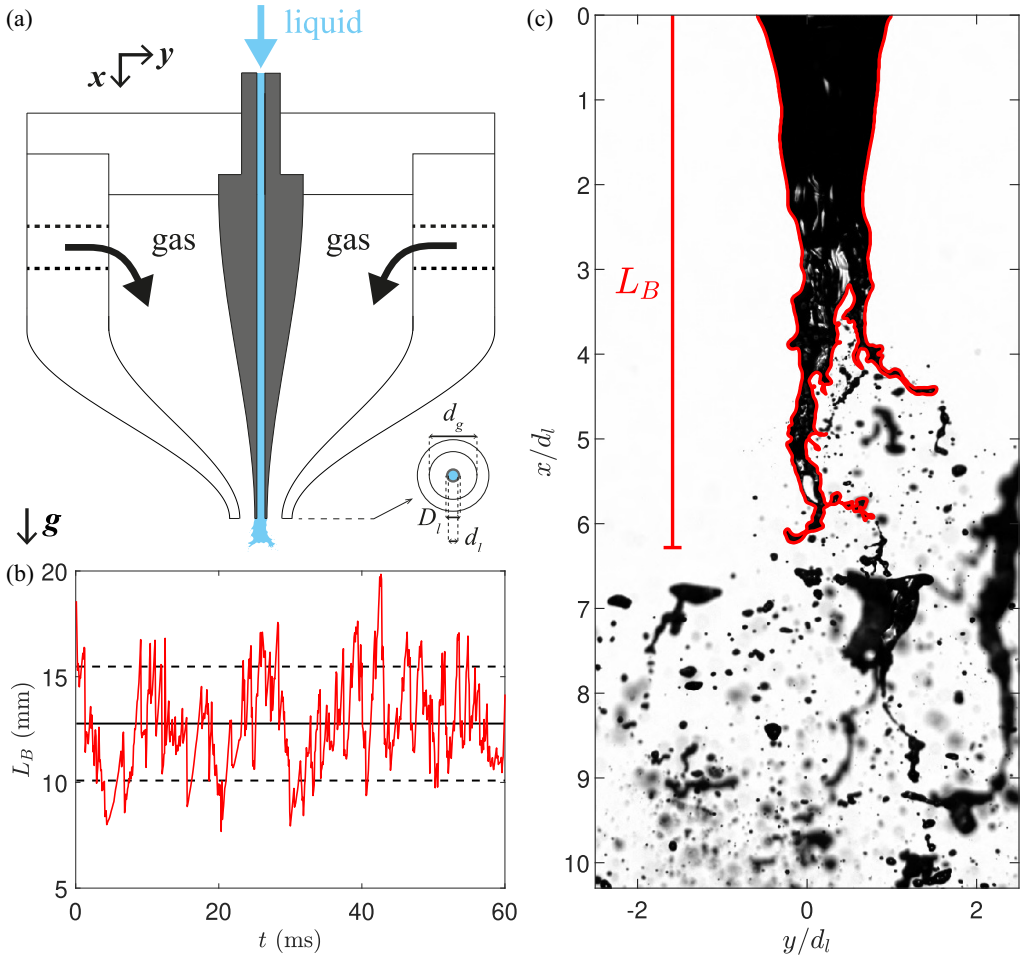
FIG. 1. (a) Schematic view of the atomizer, including a cross section of the exit plane showing the relevant dimensions. (b) Example subsample time series of liquid core length L_B. (c) Detection of the liquid core length on an instantaneous image.

Reynolds number $\mathrm{Re}_g = \frac{2Q_g}{\sqrt{\pi A_g}\nu_g}$, with ν_g the kinematic viscosity of air, ranges from 10^4 to 10^5.

The Weber number based on the gas velocity and on the liquid inner diameter $\mathrm{We}_g = \frac{\rho_g U_g^2 d_l}{\sigma}$ ranges from 14 to 950. Note that with the ρ_g and σ being fixed, the gas Weber number and gas Reynolds number can be used equivalently to describe changes in gas velocity. Alternatively, when defined based on a slip velocity between each phase, the Weber number $\mathrm{We}_r = \frac{\rho_g(U_g-U_l)^2 d_l}{\sigma}$ range becomes $11 \leqslant \mathrm{We}_r \leqslant 940$. An important dimensionless parameter for the liquid core length is the gas-to-liquid dynamic pressure ratio (also called gas-to-liquid momentum ratio) $M = \frac{\rho_g U_g^2}{\rho_l U_l^2}$, where ρ_l is the density of the liquid phase. The dynamic pressure ratio varies by over four orders of magnitude, from 0.02 to 230. The extrema of the investigated parameter space are summarized in Table I. With these injection conditions, we observe two different breakup regimes referred to as fiber-type regime, see Figs. 2(a) and Fig. 2(b), and membrane-breakup regime, see Fig. 2(c). Note that conditions where both membrane formation and fiber-type atomization can occur will be

TABLE I. Sample from the 93 investigated operating conditions, with their corresponding dimensionless parameters. The maximum and minimum values of the gas-to-liquid dynamic pressure ratio $M = \frac{\rho_g U_g^2}{\rho_l U_l^2}$, the liquid Reynolds number $\mathrm{Re}_l = \frac{U_l d_l}{\nu_l}$, and the gas Reynolds number $\mathrm{Re}_g = \frac{4Q_g}{\sqrt{4\pi A_g} \nu_g}$ are highlighted in bold. $m = \frac{\rho_l U_l A_l}{\rho_g U_g A_g}$ represents the liquid mass loading and $\mathrm{We}_g = \frac{\rho_g U_g^2 d_l}{\sigma}$ the Weber number based on the liquid diameter.

U_l (m/s)	U_g (m/s)	M	Re_l	Re_g	m	We_g
10	41.9	**0.019**	20 000	26 000	0.34	53
0.39	177	**230**	730	110 000	0.0031	950
0.39	113	94	**730**	71 000	0.0048	390
11	113	0.13	**20 000**	71 000	0.13	390
2.3	20.9	0.095	4300	**13 000**	0.15	14
1.6	177	13.3	3000	**111 000**	0.013	950

referred to as a transitional regime, since both breakup mechanisms coexist. The determination of atomization regimes is discussed in Sec. V.

B. Data acquisition

We use back-lit imaging with a high-speed camera to measure the dynamics of the liquid jet breakup. The imaging parameters are adapted to the temporal and spatial scales of the spray formation mechanisms that vary on the considered parameter space. The frame rate used ranges from 12 000 to 35 000 Hz and the imaging window varies from 20×10 to 80×30 mm^2. As the highest frame rates require reducing the number of pixels used, maintaining the targeted physical size of the imaging window is attained by lowering the magnification. The resulting spatial resolutions hence vary from 15 to 80 μm/pixels. Each movie contains at least 10^4 frames, corresponding to 0.3–0.8 s depending on the frame rate, ensuring each acquisition is longer than a hundred times the timescale associated with the liquid jet length variations.

The image processing aims at measuring the liquid core length. Each frame goes through a normalization process, which consists in substracting a reference background and then dividing by the reference background. Figures 2(a), 2(b), and 2(c) show normalized snapshots for different injection conditions. Movies of these three conditions are provided in the Supplemental Material [29]. The images are then binarized using thresholding to detect the liquid core. More details on the image processing can be found in Ref. [24]. The liquid core length L_B is then measured on each binarized image as the longitudinal extent of the detected object [see example in Fig. 1(c)].

C. Statistics and dynamics of the liquid core length

Probability density functions (PDF) are computed for each condition to describe the statistics of the liquid core length. Figure 2(d) shows the PDF for three different operating conditions. The shifts of the PDFs indicate that the average liquid core length $\langle L_B \rangle$ decreases with M. This behavior is described in the literature [17,21,22]. In addition, the distribution is wider for $M = 0.4$ (black circles) than for $M = 10.7$ (red diamonds), indicating that the standard deviation seems to decrease with M as well. We discuss the evolution of the standard deviation with M in the following section. To further understand the liquid core length distributions we characterize the shape of the PDF. Figure 3 shows one probability density function with the addition of Gaussian, skew-Gaussian, and Gamma functions, whose parameters are directly obtained from the first three statistical moments of the data (no fitting parameter). The skew-Gaussian representation [see Eq. (1)], with positive skewness, captures best the distribution. This is consistent with previous results [19]. This function as well as the scaling laws for the first three moments of the PDFs, namely the average $\langle L_B \rangle$, standard deviation $L_{B,\mathrm{STD}}$, and skewness β_{L_B} are discussed in Sec. III.
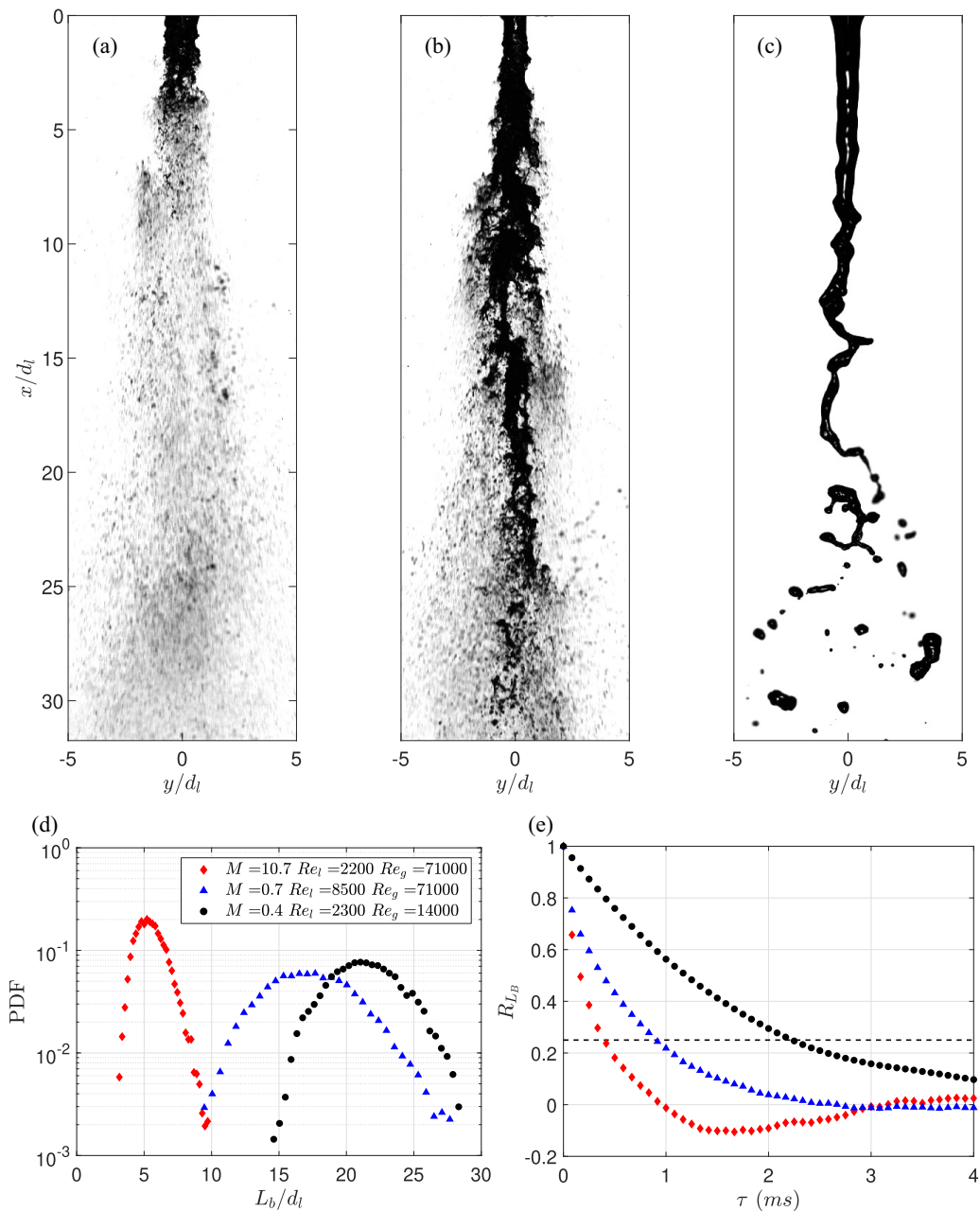
FIG. 2. [(a)–(c)] Normalized images of the jet for three different operating conditions. (a) $M = 10.7$, $Re_l = 2200$, and $Re_g = 71\,000$. (b) $M = 0.7$, $Re_l = 8500$, and $Re_g = 71\,000$. (c) $M = 0.4$, $Re_l = 2300$, and $Re_g = 14\,000$. Probability density functions (d) and autocorrelation functions (e) computed for the three injection conditions illustrated in (a), (b), and (c).

The autocorrelation function $R_{L_B}(\tau) = \langle L_B(t)L_B(t + \tau)\rangle/\langle L_B^2\rangle$, τ being the time lag, is computed to study the temporal dynamics of the liquid core length. Figure 2(e) shows the autocorrelation functions computed for three different injection conditions. Following Ref. [24], we measure a correlation time τ_c for each condition by integrating the autocorrelation function from 0 to τ_{int},
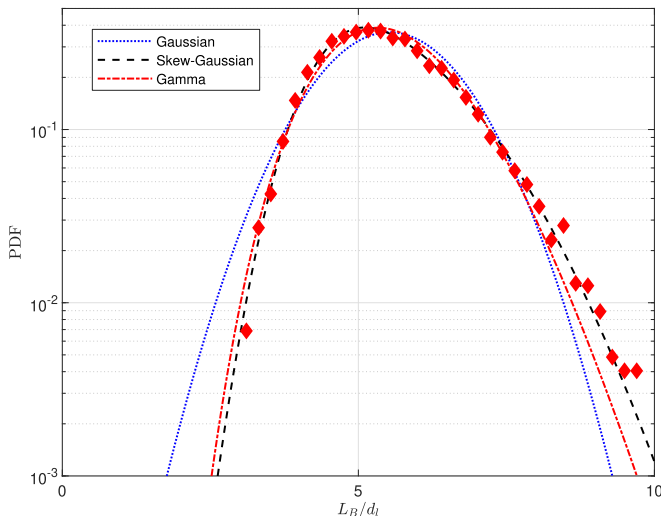
FIG. 3. Probability density function of the liquid core length normalized by the inner liquid diameter [same condition as Fig. 2(a)]. Gaussian, skew-Gaussian [see Eq. (1)], and Gamma functions are represented respectively in blue dotted line, black dashed line, and red dash-dotted line (parameters directly obtained from the first three statistical moments of the data).

τ_{int} being the time lag at which R_{L_B} crosses a threshold value of 0.25: $\tau_c = \int_0^{\tau_{\text{int}}} R_{L_B}(\tau)d\tau$, with $R_{L_B}(\tau_{\text{int}}) = 0.25$. The values of τ_c measured for $M = 10.7$, 0.7, and 0.4 (red diamonds, blue triangles, and black circles) are respectively 0.20, 0.46, and 1.2 ms. Despite a factor of 10 on the values of M of the conditions represented by the red diamonds and of the blue triangles, the autocorrelation functions and the associated measured correlation times are fairly close, compared to the large differences observed for the conditions represented by the blue triangles and the black circles, which have similar values of M. τ_c appears to have a nonmonotonous evolution with M. The shape of the autocorrelation functions and the evolution of the associated correlation time are discussed in Sec. IV.

III. STATISTICAL MOMENTS AND DISTRIBUTIONS

A. Average and standard deviation of the liquid core length

Figures 4(a) and 4(b) respectively show the average and the standard deviation of the liquid core length normalized by the inner liquid diameter, $\langle L_B \rangle/d_l$ and $L_{B,\text{STD}}/d_l$, both as a function of the gas-to-liquid dynamic pressure ratio M. In both cases, the data collapse onto a master curve. We perform power-law fits, represented by the red curve in each plot, and find them to be in good agreement with the experimental data. The prefactor and exponent obtained when fitting the normalized average liquid core length by a power law AM^n are respectively $A_{\text{avg}} = 12.8 \pm 0.8$ and $n_{\text{avg}} = -0.34 \pm 0.04$. This is consistent with previous results from the literature [21] showed that $\langle L_B \rangle$ scales with $M^{-0.3}$ on a different range of liquid Reynolds number $45 < \text{Re}_l < 300$ and for a wide range of gas-to-liquid dynamic pressure ratio $0.2 < M < 1000$, obtained by changing the density of the liquid. They report a prefactor $A_{\text{Leroux}} = 10$. References [17,22] showed that $\langle L_B \rangle$ also depends on the geometry of the nozzle, explaining the difference in terms of prefactor. The exponents they report are also in good agreement with the value found here.

The scaling of the standard deviation of the liquid core length with M was not reported before. The prefactor and exponent obtained when performing a power-law fit on $L_{B,\text{STD}}/d_l$ are respectively $A_{\text{STD}} = 2.14 \pm 0.12$ and $n_{\text{STD}} = -0.30 \pm 0.03$. The scalings of the average and standard deviation with M are almost identical, and only the prefactor of the power laws are different.
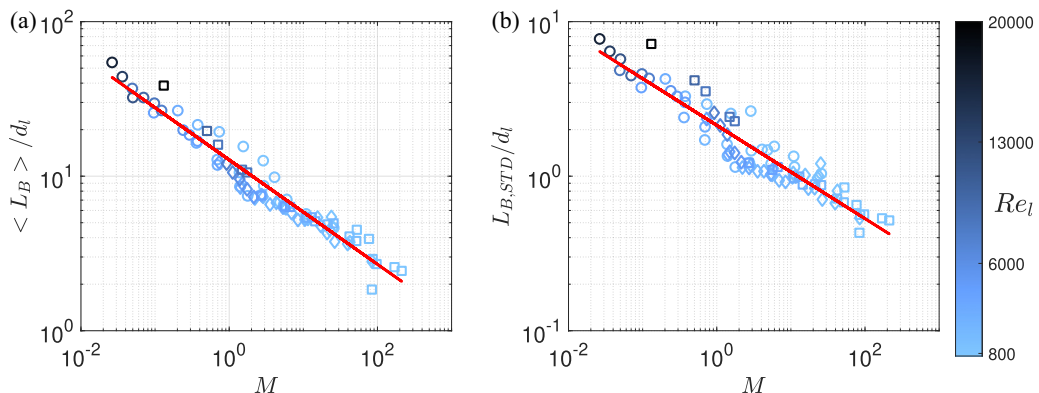
FIG. 4. Average (a) and standard deviation (b) of the liquid core length normalized by the inner liquid diameter d_l as a function of the gas-to-liquid dynamic pressure ratio M. Membrane-breakup, fiber-type breakup, and transitional regimes are represented using circles, squares, and diamonds, respectively. Power-law fits AM^n are shown in solid red line with (a) $A_{\text{avg}} = 12.8 \pm 0.8$ and $n_{\text{avg}} = -0.34 \pm 0.04$; (b) $A_{\text{STD}} = 2.14 \pm 0.12$ and $n_{\text{STD}} = -0.30 \pm 0.03$.

For both plots of Fig. 4, the membrane breakup and fiber-type atomization regimes are represented with circles and squares, respectively. In addition, diamonds are used for conditions where both membrane formation and fiber-type atomization coexist. The determination of atomization regimes is discussed in Sec. V. The liquid Reynolds number is also indicated with the color bar. No influence of atomization regimes or of Re_l is exhibited in the current dataset. The gas-to-liquid dynamic pressure ratio M is enough to capture variations of the liquid Reynolds number with a single power law for the average and standard deviation of the liquid core length L_B. M hence appears to be the sole parameter controlling the first two moments of L_B.

B. Higher-order moments of the liquid core length

To further investigate the general shape of the probability density function of the liquid core length we use the normalized and centered variable: $\tilde{L}_B = \frac{L_B - \langle L_B \rangle}{L_{B,\text{STD}}}$. Figure 5 displays the probability density functions of $\tilde{L}_B$ for every experimental conditions, showing a remarkable collapse. The black curve is a normalized and centered skew-Gaussian function, whose general expression is given in Eq. (1). It is solely defined by α, ω, and ξ, the shape, scale, and location parameters, respectively. In the case of Fig. 3, the three parameters are calculated using the first three moments of the distribution of L_B. However, the expression of the skew-Gaussian distribution is simplified in the case of a centered and normalized distribution (Fig. 5) where $\mu = 0$ and $\sigma = 1$: The shape, scale, and location parameters depend only on one parameter, the skewness, directly measured from the data. In the case of the black curve in Fig. 5, this parameter is taken as the average of the skewness value of each condition,

$$f(x) = \frac{e^{-\frac{1}{2}\left(\frac{x-\xi}{\omega}\right)^2}}{\omega\sqrt{2\pi}}\left\{1 + \text{erf}\left[\frac{\alpha(x-\xi)}{\sqrt{2}\omega}\right]\right\}, \tag{1}$$

$$\alpha = \left\{\frac{2}{\pi}\left[1 + \left(\frac{4-\pi}{2\beta}\right)^{2/3}\right] - 1\right\}^{-1/2}, \tag{2}$$

$$\omega = \frac{\sigma}{\sqrt{1 - \frac{2\delta^2}{\pi}}}, \tag{3}$$
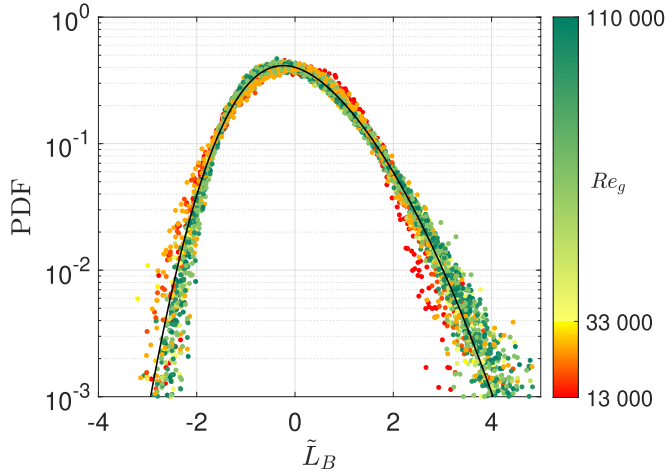
$$\xi = \mu - \omega\delta\sqrt{\frac{2}{\pi}}, \tag{4}$$

FIG. 5. Probability density functions of the centered and normalized liquid core length $\tilde{L}_B = \frac{L_B - \langle L_B \rangle}{L_{B,\text{STD}}}$ for every operating condition. The black curve corresponds to a skew-Gaussian function with zero average, unit standard deviation, and whose skewness is computed by averaging the skewness obtained for every experimental condition.

where erf is the error function, $\delta = \frac{\alpha}{\sqrt{1+\alpha^2}}$, and μ, σ, and β are respectively the average, standard deviation, and skewness.

The skew-Gaussian is in good agreement with the experimental data, confirming previous observations done in a narrower range of operating conditions [19]. Despite an apparent collapse of the curves around the average distribution (black line), close examination shows that the shape of the probability density function appears to vary slightly with the gas Reynolds number, as highlighted by the color bar. The latter emphasizes (in green) conditions for $\text{Re}_g > 33\,000$, which appear to collapse onto a master curve, while conditions of lower gas Reynolds number values behave differently. Note that in the current study, since changes in nondimensional groups only occur through changes in mean exit velocities (U_l and U_g), this transition, occurring around $U_g = 53$ m/s, is reported above in terms of gas Reynolds number for simplicity (since $\text{Re}_g \sim U_g$) but it can also be expressed with the gas Weber number with $\text{We}_g = 75$ and both threshold values will be used hereafter. To further understand these differences in shape we show in Figs. 6(a) and 6(c) the skewness of the liquid core length as a function of M and Re_g. While high dynamic pressure ratios seem to lead to a constant skewness, the behavior of β_{L_B} with M is not very clear, and the color bar highlights that Re_g seems to be a better indicator [green symbols in Fig. 6(a)]. The trend of the skewness of the liquid core length along the gas Reynolds number [Fig. 6(c)] is much clearer, as underlined by the box-and-whisker plot. The latter represents the averages and standard deviations of β_{L_B} computed in six bins spaced along Re_g. The skewness tends to be lower when $\text{Re}_g < 33\,000$ and shows an increasing trend although the spread is important. Focusing on the conditions with $\text{Re}_g > 33\,000$, we compute their average skewness, $\langle \beta_{L_B} \rangle = 0.46$, and associated standard deviation, $\beta_{L_B,\text{STD}} = 0.07$. The dashed line corresponds to $\langle \beta_{L_B} \rangle$ and the dashed-dotted lines to $\langle \beta_{L_B} \rangle \pm \beta_{L_B,\text{STD}}$. Despite a moderate spread still present above the transition, most of the data points are found to be less than a standard deviation (of the skewness) away from the average skewness. This indicates that the skewness increases with Re_g up to an asymptotic value at high gas Reynolds number, with no further dependency on other dimensionless parameters. Since the probability density functions collapse at high Reynolds numbers, higher-order statistical moments are not investigated.
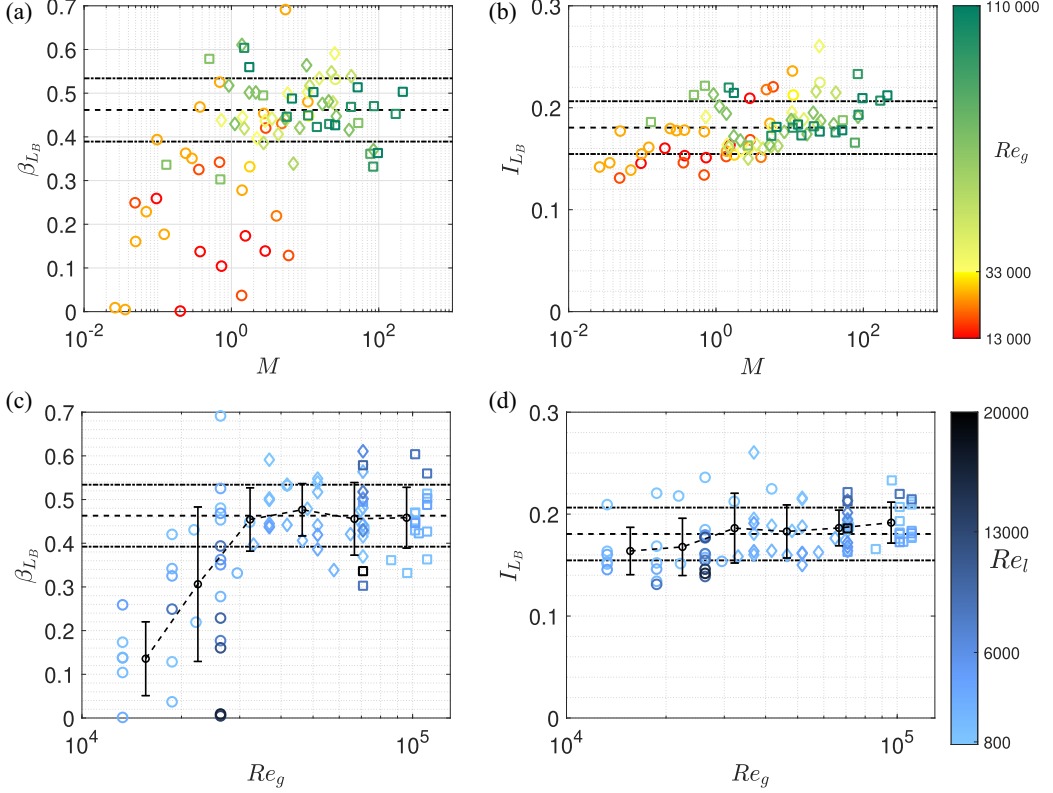
FIG. 6. Skewness of the liquid core length as a function of the gas-to-liquid dynamic pressure ratio M (a) and gas Reynolds number Re_g (c). For conditions with $\mathrm{Re}_g > 33\,000$, alternatively $\mathrm{We}_g = 75$, we compute the average skewness $\langle \beta_{L_B} \rangle = 0.46$ and the standard deviation of the skewness, $\beta_{L_B,\mathrm{STD}} = 0.07$. The dashed line corresponds to $\langle \beta_{L_B} \rangle$ and the dashed-dotted line to $\langle \beta_{L_B} \rangle \pm \beta_{L_B,\mathrm{STD}}$. Ratio of the standard deviation to the average value of the liquid core length $I_{L_B} = L_{B,\mathrm{STD}}/\langle L_B \rangle$ as a function of M (b) and Re_g (d). We compute the average and standard deviation of I_{L_B}, respectively $\langle I_{L_B} \rangle = 18.1\%$ and $I_{L_B,\mathrm{STD}} = 2.6\%$. The dashed line corresponds to $\langle I_{L_B} \rangle$ and the dashed-dotted line to $\langle I_{L_B} \rangle \pm I_{L_B,\mathrm{STD}}$. The x axes are divided into bins to compute averages and standard deviations of β_{L_B} (c) and I_{L_B} (d) to form box-and-whisker plots. Membrane-breakup, fiber-type breakup, and transitional regimes are represented using circles, squares, and diamonds, respectively.

We investigate the ratio of the first two statistical moments of the liquid core length to explore a potential signature of the transition observed on the skewness for $\mathrm{Re}_g > 33\,000$, alternatively $\mathrm{We}_g > 75$. Since both the standard deviation and the average of the liquid core length scale with $M^{-0.3}$, their ratio $I_{L_B} = \frac{L_{B,\mathrm{STD}}}{\langle L_B \rangle}$ is expected to be constant. Figure 6(b) shows I_{L_B} as a function of M. We compute the average and standard deviation of I_{L_B}, respectively $\langle I_{L_B} \rangle = 18.1\%$ and $I_{L_B,\mathrm{STD}} = 2.6\%$. The ratio of the prefactors of the fits of $\langle L_B \rangle$ and $L_{B,\mathrm{STD}}$, $\frac{A_{\mathrm{STD}}}{A_{\mathrm{avg}}} = 0.17$, is in good agreement with the value obtained for $\langle I_{L_B} \rangle$. The dashed line corresponds to $\langle I_{L_B} \rangle$ and the dashed-dotted line to $\langle I_{L_B} \rangle \pm I_{L_B,\mathrm{STD}}$. More than 60% of the conditions are within one standard deviation away from the average $\langle I_{L_B} \rangle$ and 96% the measurements are within two standard deviations of $\langle I_{L_B} \rangle$, indicating that I_{L_B} is indeed independent of M. The color bar does not indicate any further influence of the gas Reynolds number (alternatively gas Weber number) on I_{L_B}, which is confirmed by an alternate representation along Re_g in Fig. 6(d). In addition, circles, squares, and diamonds correspond to the membrane-breakup, fiber-type, and transitional regimes, respectively. No effect of the atomization regime or of the liquid Reynolds number is observed on I_{L_B}.
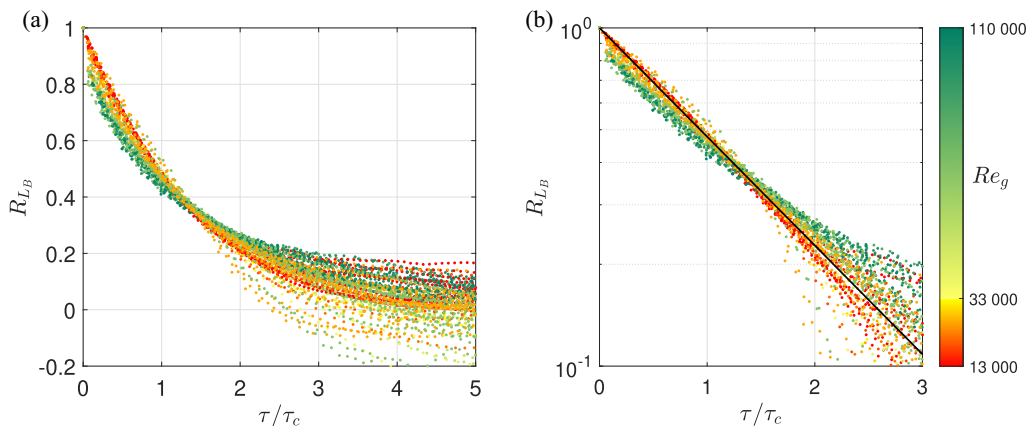
FIG. 7. Autocorrelation functions of L_B as a function of the normalized time lag $\frac{\tau}{\tau_c}$. (a) Linear ordinate. (b) Logarithmic ordinate. The black curve corresponds to $\exp(-\frac{\tau}{1.33\tau_c})$.

IV. TIMESCALES OF THE LIQUID CORE LENGTH

Figures 7(a) and 7(b) show, in linear and semilogarithmic coordinates, the autocorrelation functions obtained for each condition as a function of the normalized time lag τ/τ_c, τ_c being a correlation time obtained by a partial integration of the autocorrelation function (see Sec. II C). The color bar is the same as the one of Figs. 6(a) and 6(b) and highlights in red and green the conditions with low and high gas velocities, respectively. The solid black curve of Fig. 7(b) corresponds to the exponential function $\exp(-\frac{\tau}{1.33\tau_c})$ and captures the autocorrelation functions for conditions with low gas velocities (Re$_g$ in the vicinity of 15 000, alternatively We$_g \sim 20$). The coefficient 1.33 comes from the computation of τ_c: The time defined by the integral of a decreasing exponential function up to the crossing of 0.25 is equal to 1.33 times its exponential decay rate. Autocorrelation functions for conditions at higher gas velocities are found to initially decrease faster than an exponential function, and the initial decrease rate appears to be an increasing function of Re$_g$ in the intermediate range of gas velocities (orange to yellow symbols). This is visible by the initial ordering of the curves (for $\tau/\tau_c < 1$) where increases of Re$_g$ (red to orange to green) yield a given decorrelation over shorter time periods. For Re$_g > 33\,000$, the rate seems to reach an asymptotic value and all functions (green symbols) collapse onto a master curve. The change of shape of the autocorrelation functions of the liquid core length also highlights the transition discussed in the previous section for the distributions of L_B (around a transition value of Re$_g = 33\,000$ or We$_g = 75$): Conditions at low gas velocity are exponentially decreasing, and increases of U_g yield faster-decreasing functions, until reaching a constant decay rate after the transition, when represented along the normalized time lag τ/τ_c.

To characterize the evolution of the correlation time τ_c, we introduce a large-scale timescale of the gas jet $T_g = \frac{d_g}{U_g} \propto$ Re$_g^{-1}$. Figure 8(a) shows the correlation time normalized by the gas jet timescale $\frac{\tau_c}{T_g}$ as a function of the gas Reynolds number. We divide the range of gas Reynolds number into seven bins and compute the average and standard deviation of $\frac{\tau_c}{T_g}$ in each of these bins. The red dots correspond to the average and the errorbars to twice the standard deviation. Despite some spread, the average values do not appear to depend on the gas Reynolds number, when normalized by T_g. This shows that the correlation time τ_c scales with Re$_g^{-1}$, with a proportionality coefficient of approximately 16.3 s.

Figure 8(b) shows the correlation time normalized by the timescale of the gas jet $\frac{\tau_c}{T_g}$ as a function of the liquid Reynolds number. We divide the range of Re$_l$ into seven bins and compute the average and standard deviation of $\frac{\tau_c}{T_g}$ in each of these bins. The black dots correspond to the average and the error bars to twice the standard deviation. The normalized average values appear constant at
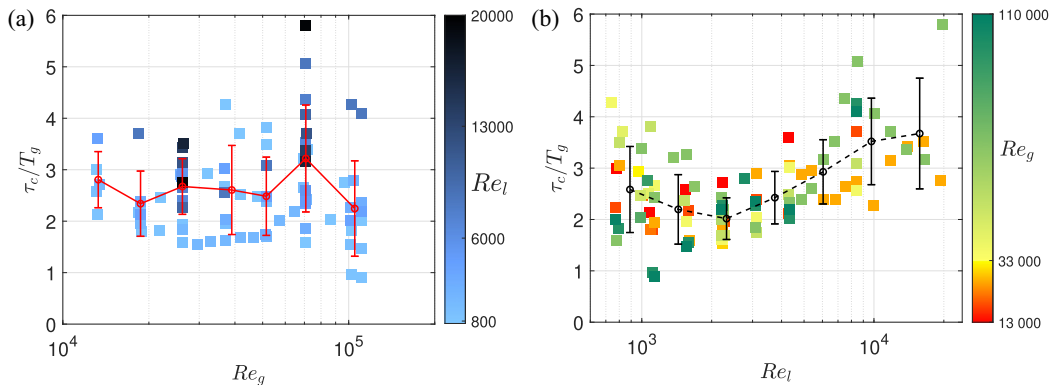
FIG. 8. Correlation time τ_c normalized by the timescale of the gas jet T_g as a function of (a) Re_g and (b) Re_l. The x axes are divided into bins to compute averages and standard deviations of $\frac{\tau_c}{T_g}$ to form box-and-whisker plots.

lower liquid Reynolds number values and finds higher values in the range of high Re_l (where a growing or constant trend remains indefinite with the current range explored). We compute the average and standard deviation for all conditions with $Re_l < 4000$ and find $\frac{\tau_c}{T_g} = 2.3 \pm 0.7$, while $Re_l > 8000$ yields $\frac{\tau_c}{T_g} = 3.6 \pm 0.9$. The change between both behaviors being gradual along Re_l and moderate in amplitude, we cannot establish a clear threshold value of liquid Reynolds number for this transition. The averaged trend highlighted by the black dashed line shows an increase starting between $Re_l = 2000$ and 4000 that may reach an asymptotic value for $Re_l \geqslant 10\,000$.

V. DISCUSSION

Figure 4 shows that the gas-to-liquid dynamic pressure ratio M is the sole parameter controlling the first two moments of the probability density function of the liquid core length. The scaling laws for the average $\langle L_B \rangle$ and the standard deviation $L_{B,\mathrm{STD}}$ of the liquid core length are power laws of M with approximately the same exponents and hence present a constant ratio. Thus, if Gamma functions were used to describe the probability density functions, the rate parameter defined as $b_\Gamma = \langle L_B \rangle / L_{B,\mathrm{STD}}$ should be constant and the shape parameter defined as $a_\Gamma = \langle L_B \rangle^2 / L_{B,\mathrm{STD}}$ should depend on M only. With this representation, one obtains the skewness directly as $2/\sqrt{a_\Gamma}$, implying a scaling with $M^{0.19}$ over the entire range of explored parameters. The observed variations of the skewness with Re_g [Fig. 6(c)] therefore cannot be reconciled when using Gamma distributions to provide a reduced description of the liquid core length distributions. Thus we conclude that skew-Gaussian distributions provide the adequate framework to describe the liquid core length statistics, confirming previous observations [19] and extending them to a much wider range of liquid and gas Reynolds numbers (equivalently gas-to-liquid dynamic pressure ratio). This representation effectively reduces the full statistics to three parameters: the average, the standard deviation, and the skewness, which directly become only two parameters given that the ratio of the standard deviation to the average liquid core length $L_{B,\mathrm{STD}}/\langle L_B \rangle$ is constant.

The first parameter describing the full statistics is the average liquid core length, which is solely controlled by one dimensionless parameter: the gas-to-liquid dynamic pressure ratio M. The second parameter corresponds to the skewness of the liquid core length, associated with the shape of the distributions. While the PDFs of $\tilde{L}_B$ first appear to collapse onto a single curve, associated with a constant skewness, closer inspections reveal a richer behavior (Fig. 5). Two regimes are underlined, governed by the gas Reynolds number, with a transition in the vicinity of $Re_g = 33\,000$, alternatively $We_g = 75$. For higher values of Re_g, the skewness β_{L_B} appears constant with $\beta_{L_B} = 0.46 \pm 0.07$, see Fig. 6. Due to experimental constraints, fewer points were obtained for low gas Reynolds numbers

and high liquid Reynolds numbers. While the imaging location can readily be chosen to be centered around the average value of L_B, high Re_l and low Re_g values would yield very low values of M and hence a very large standard deviation. Capturing the full range of the liquid core length variations would then require a very large field of view, which comes at a cost of spatial resolution and makes the detection of the liquid core challenging. Note also that conditions at both low Re_l and Re_g are outside of the studied breakup regimes. Despite the spread associated with the third-order statistical moment, for $Re_g < 33\,000$, the skewness seems to increase with Re_g toward an asymptotic value reached at $Re_g = 33\,000$ and, alternatively, $We_g = 75$ [Fig. 6(c)]. For low values of Re_g, small values of β_{L_B} are systematically found, while close to the transition, values can be found anywhere between 0 and approximately 0.5. On the contrary, for high gas Reynolds numbers, most of the value of the skewness are found within one $\beta_{L_B,\text{STD}}$ of the asymptotic value $\langle \beta_{L_B} \rangle$. This explains why when displaying every distribution of the centered and normalized liquid core length $\tilde{L}_B$ (Fig. 5), a master curve is highlighted only for high gas Reynolds (Weber) number values, while the PDF for lower values are found anywhere between a unit normal distribution ($\beta_{L_B} = 0$) and the master curve. Note that investigating this transition and the trend of β_{L_B} through the gas-to-liquid dynamic pressure ratio M is not found appropriate [Fig. 6(a)] since it seems to solely depends of the gas velocity U_g, i.e., independent of the liquid velocity U_l [Fig. 6(c)].

In opposition to the skewness, the autocorrelation functions of L_B (Fig. 7) are very well converged in the range of short time lags. The high-speed imaging measurements besides well resolve that range so that even slight change of function shape can be interpreted. Both autocorrelation functions and statistical distributions of L_B show very similar behaviors in the evolution of their shape. Starting from a decreasing exponential function at low gas Reynolds number [highlighted by the dashed line representing $\exp(-\frac{\tau}{1.33\tau_c})$], the decay rate increases slightly with Re_g (i.e., autocorrelation functions decreasing faster than an exponential) until reaching a master curve for conditions with $Re_g > 33\,000$. We conclude that the reported transition separates two regimes: (i) for $Re_g < 33\,000$, the liquid core length presents correlations and statistics with a lower decay rate and skewness than at higher gas Reynolds number and (ii) for $Re_g > 33\,000$, the statistics of L_B are described by a constant skewness while presenting correlations that decrease faster than an exponential with a fixed decay rate. With the constant ratio of the standard deviation to the average liquid core length, the statistics of L_B are described by a single parameter in the second regime and hence solely driven by M.

The transition between two regimes for the distributions and autocorrelation functions of L_B below and above the value of $Re_g = 33\,000$ (alternatively $We_g = 75$) is an unexpected finding, especially considering the reported behaviors of $\langle L_B \rangle$, $L_{B,\text{STD}}$ and τ_c, each showing a single scaling with respect to a sole nondimensional parameter (respectively, M and Re_g) over the whole range of parameters explored. A possible origin for this transition could be a change of behavior of the gas jet. Reference [30] showed that a turbulent round jet exhibits a mixing transition when the gas Reynolds number is around $Re_g \approx 10^4$. Beyond this transition, the gas jet efficiently entrains the surrounding fluid around it (ambient air in our case) and the jet's turbulent properties become drastically different. The instabilities of the liquid jet's interface originate from interactions with the turbulent gas jet surrounding it. For instance, Ref. [31] showed that increasing the gas turbulence intensity leads to interfacial instabilities presenting higher frequencies, in a planar configuration. In the same configuration, high-fidelity simulations also show a faster growth and destabilization of the instabilities when the gas turbulence is increased [32]. These interactions are thus expected to differ below and above the mixing transition of the gas jet, which in turn can be expected to play a role on the liquid core length. The increased probability of having larger values of $\tilde{L}_B$ (with respect to the average value and in proportion to the standard deviation) associated with larger skewness values, and the faster decorrelation at short times could then be explained by the difference in properties of the gas jet past its mixing transition. An in-depth characterization of the gas jet, like the work done in Ref. [30], would be required to confirm the value of the mixing transition in our situation and its link to the transition observed here at $Re_g = 33\,000$.

In an almost identical configuration, Ref. [33] reported a change of regime in the spatial gradient of the interfacial perturbation velocity around $Re_g = 45\,000$, alternatively $We_g = 190$. This supports
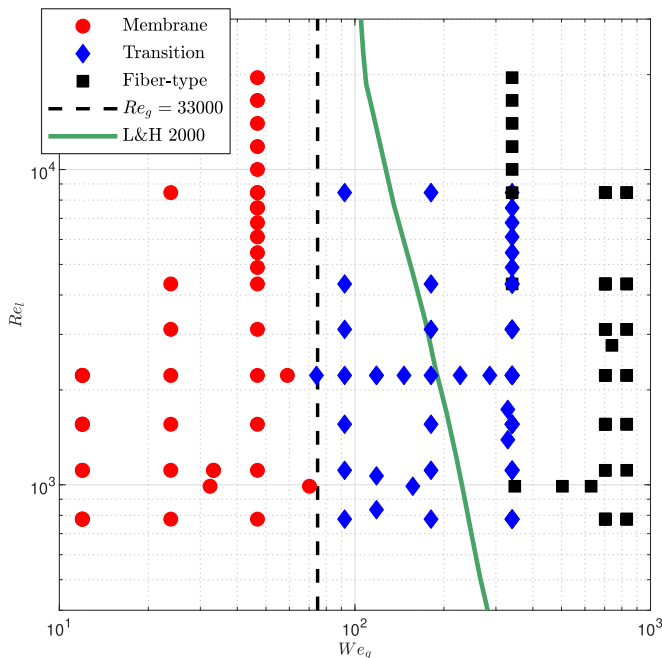
FIG. 9. Qualitative phase diagram of breakup regimes in the $\{\mathrm{Re}_l; \mathrm{We}_g\}$ parameter space. Red circles, black squares, and blue diamonds respectively correspond to membrane-breakup, fiber-type atomization, and to conditions where both of these breakup mechanisms coexist. The dashed line shows $\mathrm{We}_g = 75$ (equivalently $\mathrm{Re}_g = 33\,000$) and the green solid line corresponds to the transition reported in Ref. [15]. Note that the Weber number is defined as $\mathrm{We}_g = \rho_g U_g^2 d_l / \sigma$ in this figure.

the idea that a transition in the properties of the gas flow, thus in the interface instabilities, can participate to the change of regimes in the behavior of L_B. Reference [33] suggested that this transition is linked to a change in breakup regimes from membrane-breakup to fiber-type atomization. We investigate this by looking at a qualitative phase diagram, obtained by visual inspections of the breakup phenomena over the range of explored parameters. Figure 9 reports in the $\{\mathrm{Re}_l; \mathrm{We}_g\}$ parameter space membrane break-up, fiber-type atomization, and the transitional regime where both processes coexist. In this representation, the reported transition at $\mathrm{Re}_g = 33\,000$ corresponds to a vertical line at $\mathrm{We}_g = 75$. Thanks to the many Reynolds numbers sampled, the value of $\mathrm{Re}_g = 33\,000$ is tightly surrounded by experimental conditions. It is in good agreement with the change in atomization regimes found here, and with the transition boundary sketched in Ref. [15]. It appears that the change of behaviors presented here for $\mathrm{We}_g = 75$ occurs at the onset of fiber-type atomization, but with coexistence to the membrane formation process, while the one identified in Ref. [33] around $\mathrm{We}_g = 190$ marks the disappearance of membranes and the transition to fiber-type atomization only. Note that in both cases the boundary appears to be (almost) vertical in this diagram in the $\{\mathrm{Re}_l; \mathrm{We}_g\}$ parameter space. This means that the gas Weber number and not the relative Weber number stands as the good indicator for these transitions, since they appear to be almost independent of the liquid velocity U_l. Drawing the phase diagram in the $\{\mathrm{Re}_l; \mathrm{We}_r\}$ parameter space ($\sim \{U_l; | U_g - U_l |\}$ parameter space) would only result in a less straightforward view with oblique transitions. While a relative Weber number defined on the phase slip velocity is commonplace in multiphase flow, it seems not to be suited here, as probably noted in Ref. [15] since they use both We_g and We_r but draw the phase diagram in the $\{\mathrm{Re}_l; \mathrm{We}_g\}$ parameter space. The situation may be different and We_r may be more suited for the fragmentation of a liquid jet by a gas when the velocities of both phases are closer together, as may be interpreted by the curving

of the boundary sketched in Ref. [15], as it nears the $U_g = U_l$ line. This is the case for instance in the numerical investigations of Refs. [34,35], where We_r is used for the regime maps describing the destabilization of a planar liquid sheet segment and a transient liquid jet within a low-speed gas jet, respectively. In the case of a liquid jet surrounded by a high-speed gas jet, however, the close inspection of the statistics and temporal dynamics of the liquid core length appears as a good candidate to provide a quantitative framework to describe the transition from membrane-breakup to fiber-type atomization.

One motivation of this study was to investigate the effect of the onset of turbulence in the liquid jet on the destabilization process. Considering the statistics of L_B we report no effect of the liquid Reynolds number Re_l beyond the influence of increased liquid velocity captured by M. The correlation time, when normalized by T_g, is besides found constant for low values of Re_l [Fig. 7(b)]. However, at larger liquid Reynolds numbers the correlation time presents higher values than at low Re_l values and the increase of τ_c/T_g seems to occur between $\mathrm{Re}_l = 4000$ and $\mathrm{Re}_l = 8000$. The evolution of the normalized correlation time for high liquid Reynolds numbers is unclear and requires more conditions, exploring higher values, to be fully characterized. The unavailability of the range of high Re_l and low Re_g was described above. In addition, conditions with high Re_l and Re_g values require shorter spatial and temporal resolutions that the ones available, and would result in a very dense two-phase flow in the vicinity of the breakup, which can prevent proper identification of the liquid-gas interface [24]. One might think that the change in scaling of the correlation time above the transition is not due to the onset of liquid turbulence but simply to breakup occurring further downstream in the gas jet, where T_g does not adequately represent a characteristic timescale of the gas jet. For conditions above the transition, normalizing by a higher value of T_g (built from d_g and a value of velocity lower than U_g) for the correlation time would indeed bring the data points to the lower values found for lower liquid Reynolds numbers. Nevertheless, we know from our study of the statistics of L_B that the region where the breakup occurs is only controlled by M and breakup is found to occur only up to $5d_g$ downstream of the exit plane in the explored parameter space (even at very high Re_l values). Note that this range of breakup locations is similarly explored by conditions at lower Re_l values when Re_g is low [red points on Fig. 8(b)] which do not present higher correlation times. The gas velocity magnitude in this region is expected to still be well represented by U_g [10,36], confirming that T_g is an appropriate timescale.

We suspect that the change of behavior of the correlation time is related to the transition to a turbulent state of the liquid jet. Confirming this, however, would require velocity measurements within the liquid jet, which are challenging to implement in such setup. Lacking a clear quantitative indicator of the transition to turbulence of the liquid jet, we turn to the qualitative visualization of the liquid jet interface, as an indirect proxy to the measure of the agitation in the liquid jet. Figure 10 shows the liquid jet exiting the nozzle with no added gas flow, at $\mathrm{Re}_l = 2000$ [Fig. 10(a)], $\mathrm{Re}_l = 4000$ [Fig. 10(b)], and $\mathrm{Re}_l = 8000$ [Fig. 10(b)]. In the vicinity of the nozzle exit (i.e., at longitudinal x far from the region where the break-up due to the Rayleigh-Plateau instability occurs) the interface of the liquid jet remains undisturbed for $\mathrm{Re}_l = 2000$. We interpret this as a laminar liquid jet exiting the nozzle. The gas-liquid interface becomes slightly disturbed when $\mathrm{Re}_l = 4000$, with localized corrugations of approximately the same size. These disturbances are a signature of a deviation from a fully laminar state of the liquid jet, translating for instance the presence of turbulence spots. The situation is much different at $\mathrm{Re}_l = 8000$, as the jet is heavily disturbed by corrugations of a broad range of scales, right from the nozzle exit, a clear signature of a turbulent liquid jet. These visualizations strongly suggest that the departure from a laminar jet occurs for a value of the liquid Reynolds number found between these two bounds $2000 < \mathrm{Re}_l < 4000$, and would be the cause of the change of behavior of the liquid core length timescale. In addition, when an established turbulent state is reached so that disturbances of various sizes are observed over the whole jet, i.e., in the vicinity of $\mathrm{Re}_l = 8000$, the increase of τ_c/T_g with Re_l is seen to either saturate or become less steep [Fig. 8(b)]. Nevertheless, the color bars of Fig. 4 and Figs. 6(c) and Figs. 6(d) indicate in shades of blue the value of liquid Reynolds number and no trend is exhibited, confirming this change of regime with Re_l does not influence the moments of the probability density function.
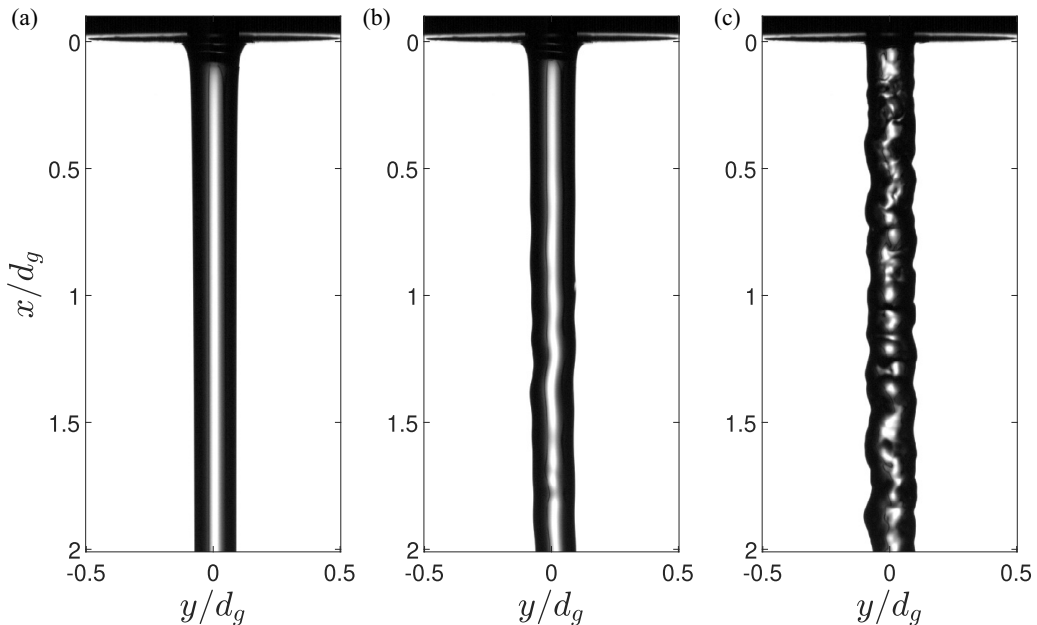
FIG. 10. Snapshot of the liquid jet exiting the nozzle in a still gas environment. (a) $Re_l = 2000$, the interface of the jet remains unperturbed in the vicinity of the nozzle and the liquid jet is laminar. (b) $Re_l = 4000$, the interface of the jet only suffers from large-scale disturbances, which suggests that the liquid jet exiting the nozzle is laminar but presents some local flow perturbations. (b) $Re_l = 8000$, the interface of the jet presents small-scale corrugations, suggesting that the liquid jet exiting the nozzle is turbulent.

In the range currently explored, the effect of the onset of turbulence in the liquid jet seems to be limited to a secondary effect on the value of the liquid core length correlation time.

VI. CONCLUSIONS

We performed high-speed back-lit imaging of the breakup of a liquid jet by a turbulent coaxial gas jet, over a wide range of liquid and gas Reynolds numbers, encompassing laminar and turbulent conditions of the liquid jet as well as two regimes of jet breakup. We focus on the liquid core length (longitudinal extent of the liquid jet, noted L_B) and study its statistics and temporal dynamics. Using autocorrelation functions of the liquid core length, we showed that the correlation time τ_c scales linearly with Re_g^{-1}. In opposition, the statistics are observed to be governed by the gas-to-liquid dynamic pressure ratio M. The average and standard deviation of the liquid core length both follow a power law with M. In addition, we find the ratio of these two statistical moments $\langle L_B \rangle / L_{B,\text{STD}}$ to be constant, effectively reducing the number of parameters needed to describe the statistics of L_B. The skewness on the other hand does not present a clear scaling with M but appears to have a nonmonotonous evolution with the gas Reynolds number Re_g. Nonetheless, thanks to a representation of the distributions of L_B with skew-Gaussian functions, we can fully describe its statistics using only two parameters: the average and skewness of L_B. The skewness is found to be constant for high Re_g, therefore further reducing the description to a single parameter in that case.

With the shape of the distributions of L_B fully characterized, we were able to identify a transition between two regimes. Conditions with $Re_g > 33\,000$ collapse on a mastercurve (Fig. 5), while conditions with $Re_g < 33\,000$ present smaller skewness values, that, despite some spread, increase with Re_g toward the asymptotic value found for high gas velocity conditions. This change of regime above and below the value of $Re_g = 33\,000$ (alternatively $We_g = 75$) is also evidenced with the

autocorrelation functions: Conditions at $Re_g < 33\,000$ show exponentially decaying autocorrelation functions, whereas for conditions with $Re_g > 33\,000$ the decay is faster than an exponential. These unexpected changes of behavior of the temporal dynamics and the statistics of L_B can be explained in the light of the mixing transition of the turbulent gas jet, found to occur around $Re_g \approx 10^4$ for round gas jets [30]. Asymptotic values of the skewness of the liquid core length as well as of the decay rate of its autocorrelation functions were exhibited and found to be reached at high gas velocity ($Re_g > 33\,000$, alternatively $We_g > 75$), where no more dependence on operating parameter exists for these metrics. The base state found at low gas velocity remains, however, to be studied, along with the on-set of the regime where these metrics depend on operating parameters. The transition in the behavior of the liquid core length seems also to be related to a change in breakup regime, from membrane-breakup to fiber-type atomization, which is qualitatively shown in the phase diagram presented in Fig. 9. The proposed framework, studying the distributions, autocorrelation functions, and their transition, appears as a candidate for a quantitative tool to describe the transition in breakup regimes.

Investigating the role of the onset of turbulence in the liquid jet on the liquid core length, we find no contribution on the statistics of L_B. However, the correlation time is shown to be proportional to a time based on the gas jet $T_g = \frac{d_g}{U_g}$, with a secondary weak dependence on the liquid Reynolds number. The values of τ_c are found in the vicinity of $2.3T_g$ at low liquid Reynolds numbers, while they neighbor $3.6T_g$ at high Re_l values. The transition between the lower and upper range of correlation time gradually happens in the range $4000 < Re_l < 8000$ through a monotonous increase. Before the increasing range, the liquid jet is laminar and is only destabilized by the Rayleigh-Plateau instability that develops further downstream ($Re_l \leqslant 2000$). Visualizations in the absence of a gas flow suggest that around $Re_l = 4000$ the liquid jet is no longer laminar, as local disturbances are observed, a potential signature of turbulent spots. For higher liquid Reynolds number ($Re_l \geqslant 8000$), the jet is heavily corrugated across a broad range of scales as it has now reached a turbulent state. We believe that the deviations from a laminar liquid jet followed by the establishment of a turbulent state are responsible for the increase in correlation time around $Re_l \sim 4000$ and its potential saturation $Re_l \sim 8000$, respectively.

As stated, the multiscale nature of spray formation prevents using a single approach to study every underlying mechanism of the fragmentation cascade. The liquid core length cannot be sufficient to fully describe gas-assisted atomization, in particular at high Weber numbers. Future work could hence encompass for instance the study of the signature of the change of atomization regimes and the onset of liquid turbulence highlighted here on other mechanisms, e.g., flapping instability, interfacial instabilities, break-up processes, and up to the droplet populations in the spray. In addition, confirming the changes of behaviors, that were observed here by varying the velocities of the fluids, but through modifications of the properties of the fluids as well would prove to be interesting future work.

[1] J. Reveillon and L. Vervisch, Analysis of weakly turbulent dilute-spray flames and spray combustion regimes, J. Fluid Mech. **537**, 317 (2005).

[2] E. Villermaux, Fragmentation, Annu. Rev. Fluid Mech. **39**, 419 (2007).

[3] J. Wen, Y. Hu, T. Nishiie, J. Iino, A. Masri, and R. Kurose, A flamelet les of turbulent dense spray flame using a detailed high-resolution vof simulation of liquid fuel atomization, Combust. Flame **237**, 111742 (2022).

[4] L. Raynal, Instabilité et entraînement à l'interface d'une couche de mélange liquide-gaz, Ph.D. thesis, Grenoble 1, 1997.

[5] P. Marmottant and E. Villermaux, On spray formation, J. Fluid Mech. **498**, 73 (2004).

[6] C. Dumouchel, On the experimental investigation on primary atomization of liquid streams, Exp. Fluids **45**, 371 (2008).

[7] A. Delon, A. Cartellier, and J.-P. Matas, Flapping instability of a liquid jet, Phys. Rev. Fluids **3**, 043901 (2018).

[8] J.-P. Matas, A. Delon, and A. Cartellier, Shear instability of an axisymmetric air–water coaxial jet, J. Fluid Mech. **843**, 575 (2018).

[9] Y. Ling, D. Fuster, G. Tryggvason, and S. Zaleski, A two-phase mixing layer between parallel gas and liquid streams: Multiphase turbulence statistics and influence of interfacial instability, J. Fluid Mech. **859**, 268 (2019).

[10] C. M. Varga, J. C. Lasheras, and E. J. Hopfinger, Initial breakup of a small-diameter liquid jet by a high-speed gas stream, J. Fluid Mech. **497**, 405 (2003).

[11] D. Fuster, J.-P. Matas, S. Marty, S. Popinet, J. Hoepffner, A. Cartellier, and S. Zaleski, Instability regimes in the primary breakup region of planar coflowing sheets, J. Fluid Mech. **736**, 150 (2013).

[12] M. Pilch and C. Erdman, Use of breakup time data and velocity history data to predict the maximum size of stable fragments for acceleration-induced breakup of a liquid drop, Int. J. Multiphase Flow **13**, 741 (1987).

[13] T. Theofanous, Aerobreakup of newtonian and viscoelastic liquids, Annu. Rev. Fluid Mech. **43**, 661 (2011).

[14] N. Chigier and Z. Farago, Morphological classification of disintegration of round liquid jets in a coaxial air stream, Atom. Sprays **2**, 137 (1992).

[15] J. C. Lasheras and E. Hopfinger, Liquid jet instability and atomization in a coaxial gas stream, Annu. Rev. Fluid Mech. **32**, 275 (2000).

[16] H. Zhao, H.-F. Liu, W.-F. Li, and J.-L. Xu, Morphological classification of low viscosity drop bag breakup in a continuous air jet stream, Phys. Fluids **22**, 114103 (2010).

[17] A. Kumar and S. Sahu, Influence of nozzle geometry on primary and large-scale instabilities in coaxial injectors, Chem. Eng. Sci. **221**, 115694 (2020).

[18] P. Huck, R. Osuna-Orozco, N. Machicoane, and A. Aliseda, Spray dispersion regimes following atomization in a turbulent co-axial gas jet, J. Fluid Mech. **932**, A36 (2022).

[19] M. Kaczmarek, R. Osuna-Orozco, P. D. Huck, A. Aliseda, and N. Machicoane, Spatial characterization of the flapping instability of a laminar liquid jet fragmented by a swirled gas co-flow, Int. J. Multiphase Flow **152**, 104056 (2022).

[20] H. Eroglu, N. Chigier, and Z. Farago, Coaxial atomizer liquid intact lengths, Phys. Fluids **3**, 303 (1991).

[21] B. Leroux, O. Delabroy, and F. Lacas, Experimental study of coaxial atomizers scaling. Part I: Dense core zone, Atom. Sprays **17**, 381 (2007).

[22] H. Zhao, H.-F. Liu, X.-S. Tian, J.-L. Xu, W.-F. Li, and K.-F. Lin, Influence of atomizer exit area ratio on the breakup morphology of coaxial air and round water jets, AIChE J. **60**, 2335 (2014).

[23] A. Kumar and S. Sahu, Liquid jet breakup unsteadiness in a coaxial air-blast atomizer, Int. J. Spray Combust. Dynam. **10**, 211 (2018).

[24] N. Machicoane, G. Ricard, R. Osuna-Orozco, P. D. Huck, and A. Aliseda, Influence of steady and oscillating swirl on the near-field spray characteristics in a two-fluid coaxial atomizer, Int. J. Multiphase Flow **129**, 103318 (2020).

[25] G. Charalampous, C. Hadjiyiannis, and Y. Hardalupas, Proper orthogonal decomposition of primary breakup and spray in co-axial airblast atomizers, Phys. Fluids **31**, 043304 (2019).

[26] G. Singh, K. Jayanandan, A. Kourmatzis, and A. Masri, Spray atomization and links to flame stability over a range of weber numbers and pressure ratios, Energy Fuels **35**, 16115 (2021).

[27] K. O. Fong, X. Xue, R. Osuna-Orozco, and A. Aliseda, Two-fluid coaxial atomization in a high-pressure environment, J. Fluid Mech. **946**, A4 (2022).

[28] N. Machicoane, J. K. Bothell, D. Li, T. B. Morgan, T. J. Heindel, A. L. Kastengren, and A. Aliseda, Synchrotron radiography characterization of the liquid core dynamics in a canonical two-fluid coaxial atomizer, Int. J. Multiphase Flow **115**, 1 (2019).

[29] See Supplemental Material at http://link.aps.org/supplemental/10.1103/PhysRevFluids.8.044304 for a video of the conditions displayed in Fig. 2, obtained using high-speed back-lit imaging.

[30] P. E. Dimotakis, The mixing transition in turbulent flows, J. Fluid Mech. **409**, 69 (2000).

[31] J.-P. Matas, S. Marty, M. S. Dem, and A. Cartellier, Influence of Gas Turbulence on the Instability of an Air-Water Mixing Layer, Phys. Rev. Lett. **115**, 074501 (2015).

[32] D. Jiang, Y. Ling, G. Tryggvason, and S. Zaleski, Impact of inlet gas turbulent intensity on the characteristics of droplets generated in airblast atomization, in *AIAA Aviation 2019 Forum* (AIAA, Reston, VA, 2019), p. 3721.

[33] G. Ricard, N. Machicoane, R. Osuna-Orozco, P. D. Huck, and A. Aliseda, Role of convective acceleration in the interfacial instability of liquid-gas coaxial jets, Phys. Rev. Fluids **6**, 084302 (2021).

[34] A. Zandian, W. A. Sirignano, and F. Hussain, Understanding liquid-jet atomization cascades via vortex dynamics, J. Fluid Mech. **843**, 293 (2018).

[35] A. Zandian, W. Sirignano, and F. Hussain, Vorticity dynamics in a spatially developing liquid jet inside a co-flowing gas, J. Fluid Mech. **877**, 429 (2019).

[36] S. B. Pope, *Turbulent Flows* (Cambridge University Press, Cambridge, UK, 2000).